Environmental Pollution 250 (2019) 1032–1043

Contents lists available at ScienceDirect

Environmental Pollution

journal homepage: www.elsevier.com/locate/envpol

# Source contribution analysis of mercury deposition using an enhanced CALPUFF-Hg in the central Pearl River Delta, China☆,☆☆,☆☆☆

Hui Xu [a], Yun Zhu [a, *], Long Wang [a], Che-Jen Lin [b], Carey Jang [c], Qin Zhou [a], Bin Yu [d], Shuxiao Wang [e], Jia Xing [e], Lian Yu [a]

[a] Guangdong Provincial Key Laboratory of Atmospheric Environment and Pollution Control, College of Environment and Energy, South China University of Technology, Guangzhou Higher Education Mega Center, Guangzhou, 510006, China
[b] Department of Civil and Environmental Engineering, Lamar University, Beaumont, TX, 77710, USA
[c] US EPA, Office of Air Quality Planning & Standards, Res Triangle Park, NC, 27711, USA
[d] Guangzhou Environmental Monitoring Centre, Guangzhou, 51000, China
[e] State Key Joint Laboratory of Environment Simulation and Pollution Control, School of Environment, Tsinghua University, Beijing, 100084, China

ARTICLE INFO

*Article history:*
Received 10 January 2019
Received in revised form
16 March 2019
Accepted 2 April 2019
Available online 6 April 2019

*Keywords:*
CALPUFF-Hg
Mercury deposition
Source contribution
Modeling
Point sources

ABSTRACT

Atmospheric mercury (Hg) poses human health and ecological risks once deposited and bio-accumulated through food chains. Source contribution analysis of Hg deposition is essential to formulating emission control strategies to alleviate the adverse impact of Hg release from anthropogenic sources. In this study, a Hg version of California Puff Dispersion Modeling (denoted as CALPUFF-Hg) system with added Hg environmental processes was implemented to simulate the Hg concentration and deposition in the central region of the Pearl River Delta (cPRD) at 1 km × 1 km resolution. The contributions of eight source sectors to Hg deposition were evaluated. Model results indicated that the emission from cement production was the largest contributor to Hg deposition, accounting for 13.0%, followed by coal-fired power plants (6.5%), non-ferrous metal smelting (5.4%), iron and steel production (3.5%), and municipal solid waste incineration (3.4%). The point sources that released a higher fraction of gaseous oxidized mercury, such as cement production and municipal solid waste incineration, were the most significant contributors to local deposition. In this intensive industrialized region, large point sources contributed 67–94% of total Hg deposition of 6 receptors which were the nearest grid-cells from top five Hg emitters of the domain and the largest municipal solid waste incinerator in Guangzhou. Based on the source apportionment results, cement production and the rapidly growing municipal solid waste incineration are identified as priority sectors for Hg emission control in the cPRD region.



## 1. Introduction

Atmospheric mercury (Hg) has been a major environmental concern for decades because of its toxicity, persistence, long-range transport, and bioaccumulation (Huang et al., 2016; Rolfhus et al., 2003; Zhou et al., 2019). It can be emitted from both natural and anthropogenic sources, and exists in three different forms in the atmosphere: gaseous elemental mercury (GEM), gaseous oxidized mercury (GOM), and particle-bound mercury (PBM). The three Hg forms undergo transport and transformations processes, then enter the biosphere through dry and wet deposition (Risch et al., 2017). Deposited Hg is then converted to highly neurotoxic methylmercury, causing health concerns. To develop mitigation measures, a better understanding of the source-receptor relationships of Hg deposition is critical.

Earlier modeling assessments of atmospheric Hg have been focused on global and regional transport and deposition caused by anthropogenic emission. Global models such as ECHMERIT (De Simone et al., 2015; De Simone et al., 2017) and GEOS-Chem (Chen et al., 2018; Wang et al., 2014) have been applied to assess the relationship between Hg emission sources and receptors at a global scale. Regional models, such as CMAQ-Hg, have been utilized

☆ School of Environment and Energy, South China University of Technology.

☆☆ Guangzhou Higher Education Mega Center, Guangzhou, China. 510006.

☆☆☆ This paper has been recommended for acceptance by Dr. Jörg Rinklebe.

* Corresponding author.
*E-mail address:* zhuyun@scut.edu.cn (Y. Zhu).

https://doi.org/10.1016/j.envpol.2019.04.008
0269-7491/

to simulate and find the primary sources of Hg deposition in the contiguous United States (Lin et al., 2012) and China (Wang et al., 2018; Zhu et al., 2015). These previous studies of Hg modeling at global and regional scales have provided valuable insight into the fate and long-range transport of atmospheric Hg (Bieser et al., 2017; Chen et al., 2014; Gbor et al., 2006; Lin et al., 2012; Sung et al., 2018). Nevertheless, the modeled values of the global, hemispheric, and regional models have largely underestimated deposition near large point sources (Chen et al., 2014; Lin et al., 2012; Wang et al., 2014). This disparity mainly arises from coarse (up to 5° using the latitude and longitude coordinate system) spatial resolution (Bieser et al., 2017; Gbor et al., 2006; Lin et al., 2007; Lin et al., 2006; Lin et al., 2012; Pongprueksa et al., 2008; Ryaboshapko et al., 2002; Sung et al., 2018; Ye et al., 2018; Zhu et al., 2015). It has been reported that there is at least a two-fold increase in dry deposition near major point sources when improving the spatial resolution from 100 km to 20 km (Pai et al., 2000). Subsequently, Pongprueksa et al. (2008) suggested that using a finer (12 km versus 36 km) spatial resolution better resolves the simulated deposition, especially near the major emission sources. Point sources accounted for an overwhelming majority of Hg emission, and their influence on near-field Hg pollution has caused concern because a high dose of Hg might lead to exposure risk to human or wildlife (Carravieri et al., 2018; Driscoll et al., 2013; Huang et al., 2016). To accurately capture the enhanced Hg pollution near large point sources and analyze the sources of Hg for such polluted sites, a higher resolution is needed.

Hg emission sources in the Pearl River Delta (PRD) region are primarily located in central area, i.e., Guangzhou, Foshan, and Dongguan (Huang et al., 2016; Ying et al., 2017; Zhang et al., 2015). Another approach for source apportionment is through statistical receptor modeling, which needs the multiple measurements at receptor's location and backward trajectory modeling analysis. Previous studies have applied multivariate receptor models such as chemical mass balance (CMB) and positive matrix factorization (PMF), and back trajectory models including potential source contribution function (PSCF), gridded frequency distributions (GFD), and concentration-back trajectory models (Cheng et al., 2015; Michael et al., 2016). However, this application is required intensive long-term air monitoring, simultaneous measurements of speciated Hg and ancillary pollutants. Therefore, for the central PRD region that lacks relevant continuous monitoring data, a dispersion model capable of tracking point source emissions, such as CALPUFF, AERMOD, and HY-SPLIT, is more suitable for its Hg simulation and source apportionment. Such dispersion models have been used in earlier studies to evaluate the dispersion, dry deposition, and spatial distribution of Hg from a major point source (Garcia et al., 2017; Heckel and LeMasters, 2011; Landis et al., 2004). However, these studies did not consider wet deposition and chemical transformation of Hg. Moreover, there have been few studies under the scenarios of multiple point sources in an industrial zone. Therefore, modeling efforts with higher spatial resolution and chemical transport processes are needed to better understand the emission transport of atmospheric Hg near point sources.

In this study, the official release of CALPUFF (v7.0) was modified to include Hg transformation and deposition processes (CALPUFF-Hg) in flue gases and polluted airsheds. Modeling assessments using the 2014 emission inventory in China and boundary conditions generated by modeled CMAQ-Hg (Liu et al., 2019) were performed to estimate the Hg deposition and the source contribution in the central region of PRD (cPRD). The model results were evaluated with observations, and then compared to the CMAQ-Hg results simulated by Liu et al. (2019) to evaluate the performance of near-field deposition. For the first time, the CALPUFF model was applied to simulate and identify sources of Hg pollution with a 1 km × 1 km resolution in a typical industrial zone of cPRD.

## 2. Methodology

CALPUFF-Hg was utilized to simulate the chemical transport of atmospheric Hg (Fig. 1). The algorithms for the transport, deposition, and fundamental chemical reactions of atmospheric Hg were added to the enhanced CALPUFF. The CALPUFF-Hg used the emission inventory of the cPRD region, meteorological data and the CMAQ-Hg results developed in our previous study (Liu et al., 2019), but with a higher grid resolution. The CMAQ-Hg model results were utilized to generate the boundary conditions (BCON) to provide a more realistic atmospheric oxidant concentrations as well as Hg concentration field for assessing the influence of Hg transboundary transport for CALPUFF-Hg. The CMAQ-Hg results were also used for comparison with CALPUFF-Hg. The source contributions on both regional and grid-cell levels were quantified using a widely used "brute force" approach (Wu et al., 2018).

### 2.1. Modification of the CALPUFF model

The CALPUFF model (http://www.src.com/) is a non-steady-state model-dependent Lagrange puff model, which was recommended by the U.S. EPA for assessing primary, secondary, toxic pollutants and their impacts from several to hundreds of kilometers' transport. The modeling system consists of three main components: (1) CALMET, a diagnostic three-dimensional meteorological preprocessor which generates meteorological fields from mesoscale meteorological models; (2) CALPUFF, an air quality dispersion model; (3) CALPOST, a post-processing package which is used for CALPUFF simulations.

#### 2.1.1. Chemistry reactions

The oxidation mechanisms of Hg in the atmosphere were not fully understood yet, which resulted in uncertainties of simulations results of Hg chemical transport models (Ariya et al., 2015; Gencarelli et al., 2017; Pacyna et al., 2016; Travnikov et al., 2017). The studies about oxidation chemical mechanisms commonly implemented in models showed that the elevated surface concentration with the oxidation by ozone and OH mechanism was better reproduced and the bromine chemistry was capable of simulating the oxidized Hg with respect to the upper troposphere and the marine boundary (Ariya et al., 2015; Bieser et al., 2017; Horowitz et al., 2017). However, observational data about atmospheric bromine concentration were limited (Kos et al., 2013; Travnikov et al., 2017), Holmes et al. (2010) indicated the bromine concentration at lower altitudes (<5km) of 20°N-30°N was less than 0.01 ppt. Moreover, Hong et al. (2016) suggested that ozone and OH oxidation dominated the GOM formation under the polluted conditions in urban areas of China, especially in the cPRD where suffered severe ozone production pollution (Ma et al., 2017). Therefore, it is representative in reflecting the chemical processes of Hg in the cPRD to incorporate the elementary gaseous phase oxidation of GEM by ozone and hydroxyl radical into default CALPUFF model, as well as in combination with the transport and deposition of Hg species. The oxidation scheme incorporated into CALPUFF-Hg is based on the first-order kinetics:

$$\boldsymbol{d}\left[\mathbf{Hg^0}\right]\Big/\boldsymbol{dt} = -\left(\mathbf{k_{o_3}}[\mathbf{O_3}] + \mathbf{k_{OH}}[\mathbf{OH}]\right)\left[\mathbf{Hg^0}\right] \quad (1)$$

where, $[\mathbf{Hg^0}]$, $[\mathbf{O_3}]$, and $[\mathbf{OH}]$ represent the concentration of $Hg^0$, ozone, and OH. $k_{O_3}$ and $k_{OH}$ are the reaction rates of $Hg^0$ oxidation by ozone and OH, referred to the studies of Hg oxidation, $3.0 \times 10^{-20}$ $cm^3$ $molec^{-1}$ $s^{-1}$ (Bullock and Brehme, 2002; Lin et al., 2007; Lin

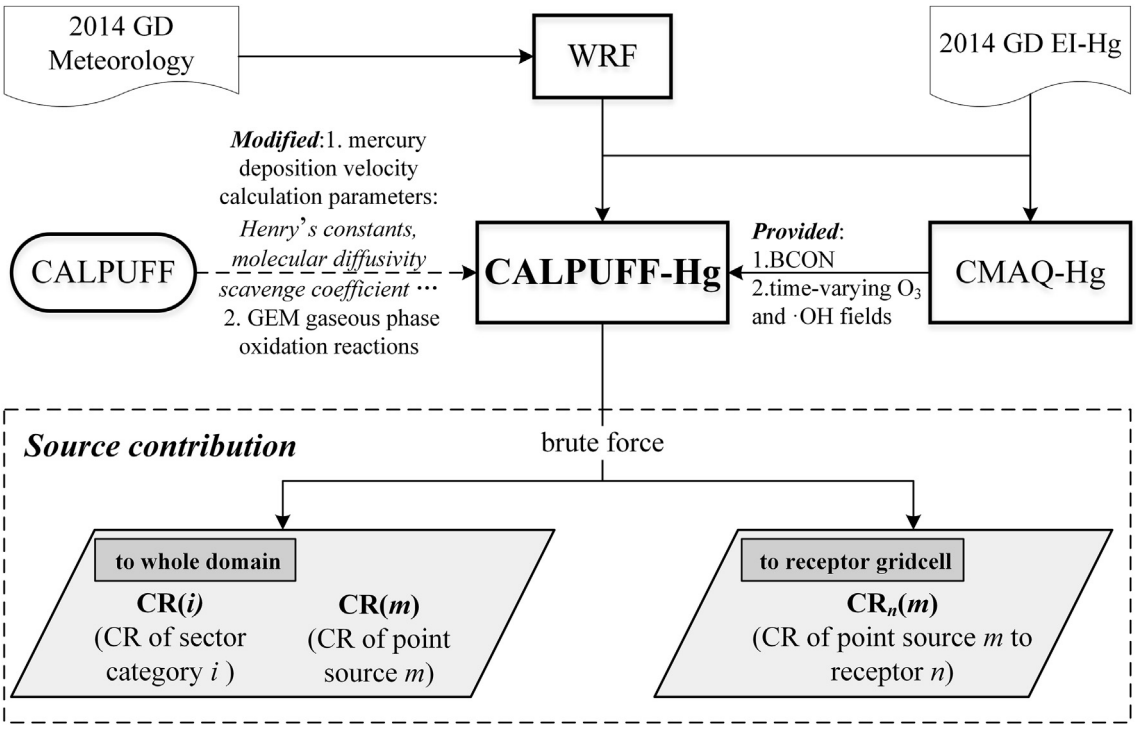


**Fig. 1.** The framework of CALPUFF-Hg model and source contribution of mercury deposition. GD: Guangdong Province, EI-Hg: emission inventory of mercury, BCON: boundary conditions, CR: contribution ratio.

et al., 2006; Ryaboshapko et al., 2002) and $8.7 \times 10^{-14}$ $cm^3$ $molec^{-1}$ $s^{-1}$ (Bullock and Brehme, 2002; Gbor et al., 2006; Lin et al., 2007; Lin et al., 2006) were chosen, respectively (shown in the Table S1). Then the model was recompiled, denoted as CALPUFF-Hg. The time-varying ozone and hydroxyl radical concentration fields generated by CMAQ-Hg were used for the CALPUFF-Hg model.

### 2.1.2. Parameters in deposition calculation

The deposition of gases and particulate Hg was simulated in the CALPUFF-Hg as the same manner as for other pollutant species previously resolved in the standard CALPUFF. A multi-layer resistance model is provided in CALPUFF for the computation of dry deposition rates of gases and particulate. The detailed descriptions of formulations are shown in Supporting Information (SI) and Table S2. The parameters, such as the Henry's constants and molecular diffusivity for gaseous pollutants, and the geometric mean diameter, the geometric standard deviation for particles in the control file (to determine the estimated dry deposition velocity) have been appended referred to the properties of Hg species. For the Henry's law constant and diffusivity, the values were 0.11 M $atm^{-1}$ and 0.1194 $cm^2$ $s^{-1}$ (Bullock and Brehme, 2002; Gbor et al., 2006; Lin and Pehkonen, 1999; Massman, 1999; Ryaboshapko et al., 2002) for GEM. An additional leaf mesophyll resistance of 25 s $cm^{-1}$ was set, which has been suggested to add mesophyll resistance for this low water solubility species (Gbor et al., 2006). For GOM, the deposition properties of $HgCl_2$ were used because it has been indicated that the most dominant aqueous $Hg^{2+}$ species is $HgCl_2$ (Lin et al., 2006), with an assumed Henry's law constant of $1.4 \times 10^6$ M $atm^{-1}$ (Bullock and Brehme, 2002; Lin and Pehkonen, 1999; Ryaboshapko et al., 2002) and diffusivity of 0.086 $cm^2$ $s^{-1}$ (Lin et al., 2006). Moreover, the reactivity of GEM and GOM was set as 2 and 18, respectively, according to the CALPUFF model's recommended values of NO and $HNO_3$ due to the similar water solubility. For Hg particles, the geometric mean diameter of 0.48 μm and the geometric standard deviation of 2.0 μm had been given followed the recommended values of (Xu et al., 2000) in CALPUFF.

Wet deposition of Hg was mainly from GOM and PBM, and GEM was negligible in this paper due to its low solubility in water. The formulation of wet removal is described in SI. The main parameter is the scavenging coefficient, a fixed one set at $6.0 \times 10^{-5}$ $s^{-1}$ in liquid precipitation for GOM which is the same as that for $HNO_3$, as they have the similar aqueous solubility (Voudouri and Kallos, 2007; Xu et al., 2000). The scavenging coefficient of 0 in frozen precipitation was set for GOM because Sigler et al. (2009) has reported that snowfall has little effect on ambient GOM. While in liquid or frozen precipitation state for PBM, the values were chosen as $1.0 \times 10^{-4}$ $s^{-1}$ and $3.0 \times 10^{-5}$ $s^{-1}$, respectively, following the parameters of $SO_4^{2-}$ (Xu et al., 2000) in CALPUFF.

## 2.2. Model simulations

### 2.2.1. Study domain and meteorology

The CALPUFF-Hg model domain is in Lambert Conformal projection over the cPRD, an area specified between 22.49°N and 23.63°N, 112.66°E and 114.44°E. It contains 128 × 180 grid cells with a spatial resolution of 1 km × 1 km and 10 vertical layers: the entire Dongguan (DG), most of Guangzhou (GZ), Foshan (FS), Shenzhen (SZ), and part of Huizhou (HZ), Zhaoqing (ZQ), Jiangmen (JM), Zhuhai (ZH) are also included in the domain (Fig. 2).

Meteorological fields for driving CALPUFF-Hg was generated from Weather Research and Forecasting Model (WRF version 3.9.1) and obtained from our previous work (Liu et al., 2019). The WRF output was reformatted by CALWRF and then preprocessed by CALMET for subsequent CALPUFF-Hg simulation. Hourly meteorological data was input for CALPUFF-Hg and the modeling period was the entire year of 2014.

*2.2.2. Emission inventory*

The anthropogenic emission inventory used for CALPUFF-Hg modeling was the updated emission inventory of Guangdong province in 2014 developed by Liu et al. (2019), which was based on the work of Wu et al. (2016). The natural emission obtained from Wang et al. (2016b) was included in the Hg emission inventory. The total anthropogenic emissions are 8301 kg, the propagated uncertainty mainly contributed by coal, metal concentrates, and limestone for Hg emission estimates was (-19%, 22%) with the 80% confidence interval (Wu et al., 2016). Among the anthropogenic emission, the emissions from the anthropogenic point sources account for 99.9% and were classified into seven categories for source apportionment analysis: (1) emissions from coal-fired power plants (CFPP), (2) emissions from municipal solid waste incineration (MSWI), (3) emissions from cement production (CEM), (4) emissions from non-ferrous metal smelting (NONF), (5) emissions from iron and steel production (IASP), (6) emissions from paper-making production (PM), and (7) emissions from other point sources (OTHER), such as cremation, battery production, etc. The monthly variation of anthropogenic point sources was configured according to the monthly thermal power generation and product yields of Guangdong in 2014 obtained from the National Bureau of Statistics. Table 1 shows the emissions from these point sources and the speciation profiles for each category. There were 2221 plants with 8296 kg of total mercury (THg) emissions in CALPUFF-Hg domain. The largest emitter is CFPP, with an amount of 2647 kg $yr^{-1}$ (31.9%) and the top three categories (CFPP, CEM, and NONF) make up the majority (75.2%) of total point sources emissions. Hg speciation from anthropogenic sources varies due to many factors including coal composition, combustion technologies, removal efficiency for different Hg species in atmospheric pollution control devices (APCDs). The specific speciation profiles (Chen et al., 2013a; Wu et al., 2016; Zhang et al., 2015) used for CALPUFF-Hg are shown in Table S3. The profiles are consistent with the previous study of PRD (Zheng et al., 2011) except MSWI, CEM, and IASP, which are from the measured results of municipal solid waste incinerators, cement plants, iron and steel plants in PRD or China. In terms of spatial distribution of the point sources, Fig S1a-d displays the locations; the dot size illustrates the emission of THg and three forms of Hg. The sum of total Hg emissions from FS, GZ, and DG accounts for 76.5% of the total point sources emissions. Moreover, the different forms of Hg are also emitted principally from these cities. These three cities are the first three most important emission cities, which is the same as that reported by Huang et al. (2016).

*2.2.3. Model scenarios and data analyses*

The BASE scenario was conducted to verify the results of CALPUFF-Hg and assess the improvement at a higher resolution by comparing with CMAQ-Hg results from Liu et al. (2019). A series of model runs (CFPP, MSWI, CEM, IASP, NONF, PM, and OTHER) was made to evaluate the contributions of emissions from these different categories to Hg deposition of the cPRD. The modeling period was the entire year of 2014. The list of all above runs is given in Table 1. What's more, the point sources of seven scenarios (CFPP, MSWI, CEM, NONF, IASP, PM, and OTHER) were simulated one-by-one to consider the separate contributions of large point sources to Hg deposition in the domain. The results of 72 point sources (PS1-PS72, shown in Fig. 2, the serial number of point sources indicated the sequence of total Hg emission, e.g. PS1 was the largest THg emitter) whose emissions accounted for more than 85% of the total were selected out based on the principle of environmental statistics (MEE, 2009). In addition, to assess the influence of large point sources on their near-field Hg deposition, the nearest grid-cells (i.e., receptors, noted as RP1-RP6, shown in Fig. 2) from top five point sources and the largest MSWI in Guangzhou were investigated. The alone result of a single point source to each selected receptor was extracted by CALPOST scripts according to the rows and columns of the receptors. According to the distribution interval of Hg speciation uncertainty (Table S3), the uncertainty upper and lower limit scenarios (U1-U12, denoted as “uncertainty cases”) were set for assessing the uncertainty. Each scenario differs only in the speciation proportions of the targeted single category in the emission inventory (shown in Table S4) compared to BASE scenario for every point source category. The uncertainty cases were simulated in APR 2014 only. The same input concentration fields of ozone and hydroxyl radicals were used for CALPUFF-Hg simulations.

The source apportionment for categories and point sources to deposition of the domain, point sources to the deposition of selected receptors in the CALPUFF-Hg was based on “brute-force” (Kwok et al., 2015; Zhang et al., 2014) method, which meant that the targeted category or point source was simulated when evaluated the contribution of the category or point source. The application of this method is based on the additivity of the simulation results of each emission category. Due to the large concentration difference between GEM (e.g. 5.0 ng $m^{-3}$) and the primary oxidant (e.g. $O_3$: 100 μg $m^{-3}$), it is generally considered that the reduction of oxidant in the Hg chemical reaction is negligible. In addition, Ghannam and El-Fadel (2013) reported that CALPUFF exhibits a linear response to changes in emission rates of pollutant, even in the presence of chemical transformations. Extensive modeling assessments using both regional model (such as CMAQ-Hg) and global models (such as GEOS-Chem) have shown that simulated deposition is linearly proportional to emissions and the model results from various emission cases are additive on an annual basis (Lin et al., 2012; Liu et al., 2019; Travnikov et al., 2017; Wang et al., 2014; Zhu et al., 2015). Therefore, the method of source

**Table 1**
The specification of emission inventory and simulation scenarios.

| Scenarios | Emission Inventory | | Emissions Remarks | Descriptions |
|---|---|---|---|---|
| | Natural (kg/year) | Anthropogenic (kg/year)[a] | | |
| BASE | 2219[b] | 8301 | Emissions of all sources (including anthropogenic sources, natural sources) and boundary conditions | BASE run |
| BCON | | | Only boundary conditions | Effect of different categories |
| CFPP | | 2647 | Only emissions of coal-fired power plants | |
| MSWI | | 555 | Only emissions of municipal solid waste incineration | |
| CEM | | 2582 | Only emissions of cement production | |
| NONF | | 1008 | Only emissions of non-ferrous metal smelting | |
| IASP | | 544 | Only emissions of iron and steel production | |
| PM | | 590 | Only emissions of paper-making production | |
| OTHER | | 370 | Only emissions of other point sources | |

[a] The anthropogenic emission of the BASE is the sum of all point sources emissions (8296 kg) and area sources emissions (5 kg).
[b] Natural emissions was obtained from Wang et al. (2016b).

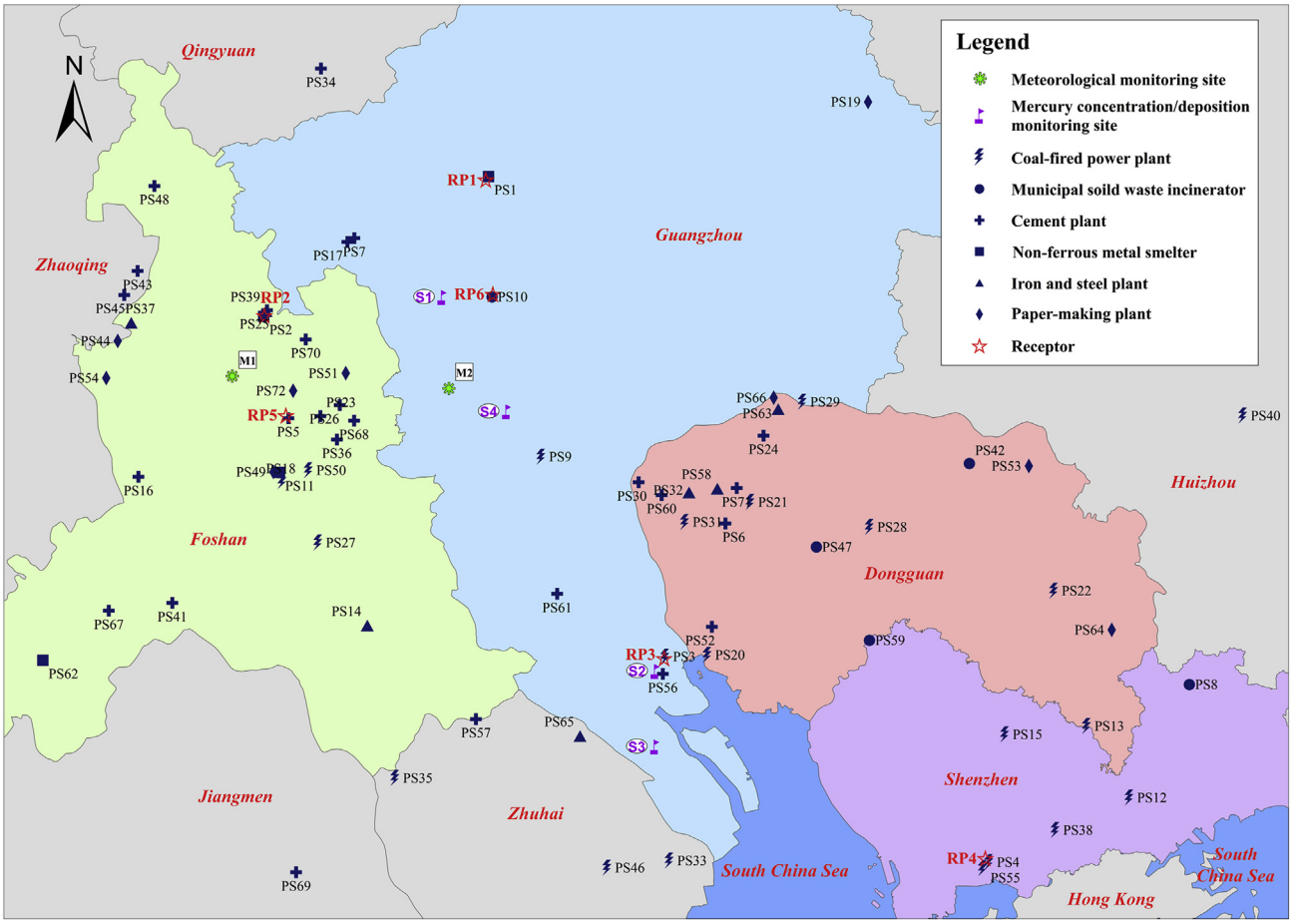


**Fig. 2.** The locations of meteorological monitoring sites (M1-M2), mercury concentration or deposition observation sites (S1-S4), major point sources (PS1-PS72) and selected receptors (RP1-RP6).

contribution assessment in this paper is plausible. The contribution of Hg deposition in the domain from sector categories $i$ (BCON, CFPP, MSWI, CEM, NONF, IASP, PM, and OTHER) is characterized as $S(i)$. In addition, the contribution of individual point source $m$ to the entire domain and single receptor grid $n$ are characterized as $S(m)$ and $S_n(m)$. The contribution ratio (CR) for each factor is therefore specified by equations (2)–(4),

$$CR(i) = \frac{S(i)}{\sum_{i=1}^{8} S(i)} \times 100\% \quad (2)$$

$$CR(m) = \frac{S(m)}{\sum_{m=1}^{2221} S(m)} \times 100\% \quad (3)$$

$$CR_n(m) = \frac{S_n(m)}{\sum_{m=1}^{2221} S_n(m)} \times 100\% \quad (4)$$

where $CR(i)$ represents the contribution ratios of Hg deposition in the whole domain from sector categories; $CR(m)$ and $CR_n(m)$ represent the contribution ratios to Hg deposition from each point source in the domain and a specific receptor grid, respectively.

The NCAR Command Language (NCL) was used for data visualization of CALPUFF-Hg a. MATLAB, Origin 8.0, and Microsoft Excel were used for presenting the analytical results.

## 3. Results and discussion

### 3.1. Model performance

#### 3.1.1. Verification of meteorological fields

The performance on temperature, wind speed, and relative humidity of the WRF model has been evaluated by comparing hourly mean simulated results with the measured values in our previous work (Liu et al., 2019). In this work, we also evaluated the precipitation of the observation sites in the cPRD region for wet deposition calculation in CALPUFF-Hg. The precipitation has a distinct seasonal pattern of wet season and dry season (mainly classified by precipitation and temperature in the Pearl River Delta (Cui et al., 2015)), the sum predicted precipitation in the wet season accounts for 72.78% of the annual precipitation while the ratio of observation is 84.14%. Combined with Fig S2 and Table S5, the scatterplot shows small variability (overestimated in the dry season and underestimated in the wet season) of simulated monthly precipitations from WRF, but it is mostly within the 0.5–2 slope limit of the wet season and similar rainfall on an annual basis (relative biases were within ±15%) between model and observation. This indicates that the WRF results appropriately reflected the realistic amount of rainfall in the cPRD and it can be used as the input for wet deposition calculation of CALPUFF-Hg and CMAQ-Hg.

#### 3.1.2. Verification of CALPUFF-Hg results

The spatial distribution of annual average Hg concentrations

simulated from the BASE scenario is shown in Fig. 3a-d. The higher concentration coincides with the locations of at the point source locations. The variation ranges of the predicted concentrations of GEM, GOM, and PBM are 2.75–8.07 ng $m^{-3}$, 0.01–1.58 ng $m^{-3}$, and 0.01–0.29 ng $m^{-3}$, respectively. GEM contributed up to 75%–99% of the THg concentration in the domain grids. These results are consistent with earlier studies (Lin et al., 2010; Wang et al., 2014; Yang et al., 2018a; Zhu et al., 2015). Reported Hg observation data from the literatures (Chen et al., 2013a; Li et al., 2011) in the cPRD region are collected for verification (Table 2). The predicted concentrations from the BASE scenario agree reasonably well with the field measurement even though the time periods of model and measurements are not synchronized. The site S4 is under-predicted by 25.22%, this is because the concentration has slightly decreased in Guangzhou urban area as some point source relocated after the implementation of "Suppress the Second Industry and Develop the Third Industry (GZEP, 2013)" at the end of 2012. In addition, unreported hourly average atmospheric Hg concentrations near two major point sources observed by a Tekran speciated Hg analyzer are shown. The sampling date was May 2014 at S1 (23.269°N, 113.323°E) and S2 (22.795°N, 113.552°E), as shown in Fig. 2. Fig. 5 shows the comparison of the modeled concentrations from BASE scenario and observed concentrations of three Hg species at S1 and S2. The boxplots show that the observed and simulated values are in close agreement. The model captures the elevated concentration at these highly polluted sites to a certain degree, for S2, the mean

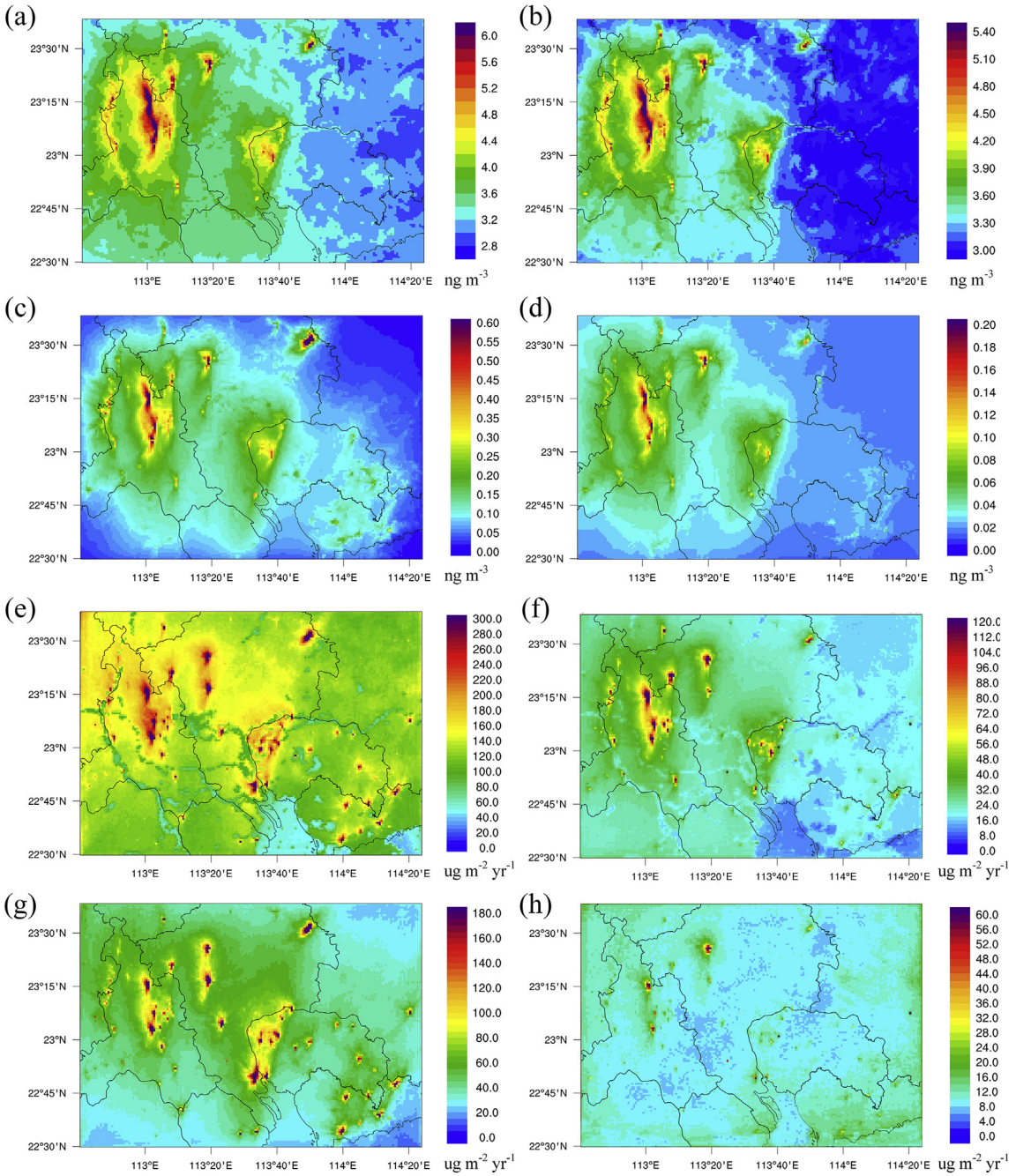


**Fig. 3.** The simulated model results of BASE scenario in 2014: concentration of (a) THG, (b) GEM, (c) GOM, and (d) PBM; deposition of (e) THG, (f) GEM, (g) GOM, and (h) PBM.

**Table 2**
Comparison of the predicted THg concentration and deposition with the field measurements in the central of PRD region.

| Sites | Site Name | Location | Sampling Period | Observation | | | Model | | | Model Value Notes | Relative Bias |
|---|---|---|---|---|---|---|---|---|---|---|---|
| | | | | Con[d] | Wet dep.[e] | Dry dep.[f] | Con | Wet dep. | Dry dep. | | |
| S3[a] | Wanqingsha | 22.7°N, 113.55°E | 11/2008–12/2008 | 2.94 | | | 3.08 | | | Nov and Dec average | 4.76% |
| S4[b] | Guangzhou | 23.124°N, 113.355°E | 11/2010–11/2011 | 4.6 ± 1.36 | | | 3.44 | | | annual average | −25.22% |
| S4[c] | Guangzhou | 23.124°N, 113.355°E | 01/2010–12/2012 | | 145.02 | 58.57 | | 117.66 | 73.95 | annual average | −18.87%/26.26% |

[a] Data from Li et al. (2011).
[b] Data from Chen et al. (2013b).
[c] Huang et al. (2016).
[d] Hg concentration (Unit: ng $m^{-3}$).
[e] Wet deposition of Hg (Unit: μg $m^{-2}$ $yr^{-1}$).
[f] Dry deposition of Hg (Unit: μg $m^{-2}$ $yr^{-1}$).

bias of THg is 0.78 ng $m^{-3}$ (mean concentration of 4.69 ng $m^{-3}$ from model compared to 3.91 ng $m^{-3}$ from measurement), resulting in the normalized mean bias (NMB) of 9.04% and normalized mean error (NME) of 43.36% for THg. The model slightly underestimates for S1 with the NMB of −41.07% and NME of 43.52% for THg. This is because that the wind was a key factor in Hg simulation near large point sources and it is difficult for accurate estimation compared to other meteorological parameters, great uncertainty would result from a tiny deflection of simulated wind direction especially in short periods at the 1 km × 1 km resolution.

The spatial distribution of modeled Hg deposition from BASE scenario is shown in Fig. 3e-h. There is a clear dividing line with the direction of the Pearl River Basin in the map, which was never shown in other literature (Liu et al., 2019) about the PRD. It is mainly because the dry deposition velocities are changed accompanied by leaf area index (LAI) in the context of there is a more realistic classification of land use types at a higher resolution. In the study domain, the THg deposition is 171.02 μg $m^{-2}$ $yr^{-1}$ (94.68 μg $m^{-2}$ $yr^{-1}$ for total dry deposition and 76.34 μg $m^{-2}$ $yr^{-1}$ for total wet deposition). The total deposition value slightly exceeds the values estimated by Lin et al. (2010), Wang et al. (2014) and Yang et al. (2018b), but it agrees well with Hg deposition value predicted by Zhu et al. (2015) with a relative bias of 8%.

The species-specific contribution to the monthly deposition estimated by BASE scenario is shown in Fig. 4. The monthly variability is mainly caused by meteorology conditions. The total deposition and sub-species deposition exhibit a difference between the wet season and the dry season. The depositions during the wet season and the dry season share 63.1% and 36.9% of the annual total deposition, respectively. The deposition in the wet season increases as the wet deposition increased, which is consistent with the report about southern China (Wang et al., 2018). It is clear that the deposition is dominated by dry deposition during the dry season (72.6% of total deposition); while the wet deposition is slightly more important during the wet season (54.9% of total deposition). PBM and GOM are the species that contributed most to the increasing total deposition in the wet season because the higher water solubility of GOM and the relatively higher scavenging coefficient of PBM bring about the corresponding increase of wet deposition with the large rainfall. In addition, the dry deposition of GEM has a slight upward trend in the wet season. It is due to the slightly elevated dry deposition rate of GEM caused by the change of LAI, width of stomatal opening, and the friction velocity; but at the same time, the clean air mass from sea (the prevailing wind direction of the PRD in the wet season was southeast, Fig S3) and vertical mixing diffusion in the wet season dilute the surface concentration of GEM and reduce the dry deposition. The combined effect makes the dry deposition of GEM show no remarked changes in seasonal variation.

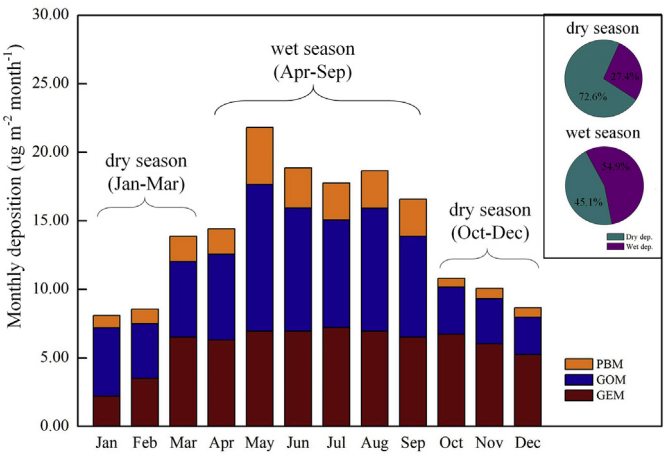


**Fig. 4.** The monthly deposition variation of each species. The pie charts show the ratios of the dry and wet deposition in the dry season and wet season in the central of PRD (Dry dep., dry deposition, Wet dep., wet deposition).

The scarcity of observations for dry and wet deposition limited the evaluation of model performance for Hg deposition in the cPRD region. Table 2 lists the Hg deposition of the site (S4, shown in Fig. 2) with the observed data (Huang et al., 2016) in the cPRD region. The estimated and measured THg deposition values are quite close. The simulated wet deposition of the site is slightly underestimated (18.87%) because of the underestimation of the predicted precipitation compared to the observed values at S4 (1210.8 mm versus 1699.2 mm). The dry Hg deposition predicted by CALPUFF-Hg is 1.26 times the reported observation value, one possible reason is the underestimation of observations due to the employed measurement method as reported by Huang et al. (2016). It can also be seen that the simulated average wet and dry deposition values of the entire domain are in the range of 8.76–76.39 μg $m^{-2}$ $yr^{-1}$ (Feng et al., 2002; Guo et al., 2008; Xu et al., 2014; Zhao et al., 2018; Zhu et al., 2014) and 34.7–293.2 μg $m^{-2}$ $yr^{-1}$ (Fang et al., 2001; Wang et al., 2016a) respectively, which have also been observed in other cities of China. The acceptable differences between model and measurements result from the uncertainty of Hg emission and the variations of meteorological conditions. Table S6 shows the concentration and deposition of the uncertainty cases. Emission speciation has a stronger impact on simulated concentration and deposition of GOM and PBM than that of GEM due to their higher deposition velocities. Speciation distribution of CFPP has the largest impact on concentration and deposition, the uncertainty intervals of GOM concentration and deposition are (-8.1%, 20.0%) and (-12.2%, 30.3%), respectively, still within the ±50% level for model performance evaluation. Overall, the simulation results appropriately reflect measured concentration and deposition of atmospheric Hg in the cPRD region.

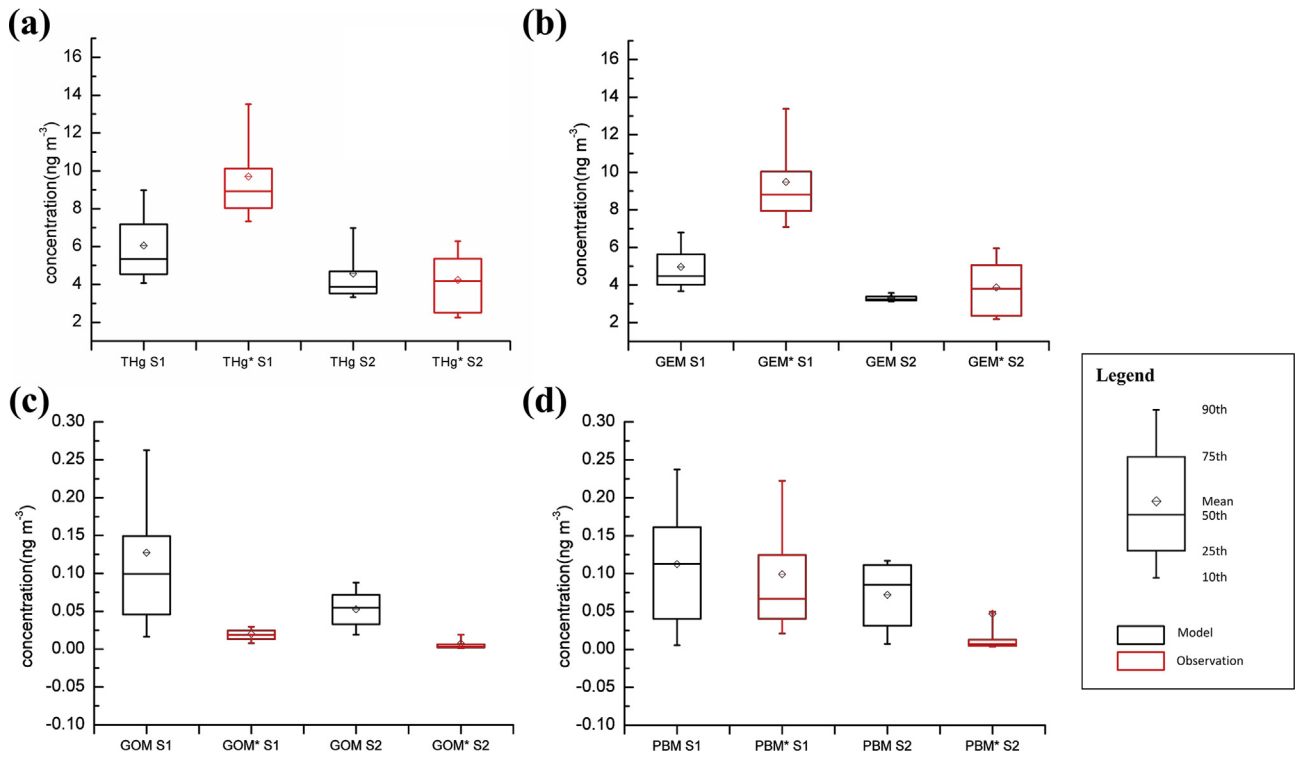


**Fig. 5.** The comparison between modeled and observed (red line marked with *) mercury concentrations of (a) THG, (b) GEM, (c) GOM, and (d) PBM in May 2014. (For interpretation of the references to colour in this figure legend, the reader is referred to the Web version of this article.)

*3.1.3. Comparison of CALPUFF-Hg and CMAQ-Hg deposition results near emission sources*

Earlier studies have put forward that the CMAQ-Hg simulation at a coarse resolution would underestimate the Hg deposition, especially near large point sources. However, whether and to what extent we can improve the underestimation with a finer 1 km × 1 km grids has never been quantified. To investigate this issue further, the simulation results of January are chosen for simulation to show the characteristics and the effects of point sources to isolate the influence of natural emission since natural emission quantity is smallest in a winter month (Lin et al., 2010; Shetty et al., 2008; Wang et al., 2018). The CMAQ-Hg results with 3 km × 3 km grid in Liu et al. (2019) were interpolated beforehand to the same 1 km × 1 km grid as the CALPUFF-Hg model.

Table S7 and Fig S4 show the special distribution of Hg concentration and deposition results of BASE and the CMAQ-Hg results (Liu et al., 2019). In general, the simulated monthly average THg concentration and deposition of CALPUFF-Hg are consistent with the regional model. The spatial distributions of both models are similar for concentration and deposition: the results show that the concentration and deposition patterns caused by the point source emissions (Fig S4). The results from CALPUFF-Hg give a smoother texture. However, the peak concentration and deposition of the CALPUFF-Hg are twice more than that of the CMAQ-Hg (Table S7), particularly near the source locations (Fig S4), which is caused by the difference in emission dilution and the capture ability of the spatial variations of two models for Hg concentration and deposition. Compared with the monthly average concentration of CALPUFF-Hg, the CMAQ-Hg results is 3.2% less while the ratio for the maximum concentration is 55.0%. In terms of the total deposition of the entire domain average, it is underestimated 4.9% on a monthly basis at the coarse resolution of CMAQ-Hg.

To clarify the spatial distribution difference of the near-field Hg deposition between CALPUFF-Hg and CMAQ-Hg model results, PS10 was chosen since there were no large point sources within 15 km of it, and the deposition values of grid-cells within a 2 km, 5 km, and 10 km radius of PS10 (its location as shown in the Fig. 2) are singled out to draw the density maps (Fig. S5). There are two differences worthy of note. First, the depositions of CMAQ-Hg show much smaller variability, while the peak deposition simulated by CALPUFF-Hg rises to above 70 $\mu g\,m^{-2}\,mon^{-1}$. Another difference is that the wave crest of the density curve for CALPUFF-Hg results is right-shifted compared to CMAQ-Hg results both in 5 km domain and in 10 km domain. In addition, in the 2 km domain, the depositions of 5 ($n = 16$) grid-cells are above 32 $\mu g\,m^{-2}\,mon^{-1}$ in the CALPUFF-Hg simulation, while there are only 3 grid-cells in the CMAQ-Hg simulation; moreover, the peak value of CALPUFF-Hg (71.48 $\mu g\,m^{-2}\,mon^{-1}$) is much larger than that of CMAQ-Hg (39.03 $\mu g\,m^{-2}\,mon^{-1}$). These phenomena imply that the simulated Hg deposition of CALPUFF-Hg is higher and the high value occurrs at a higher frequency in the same domain near the point source. These results show that CALPUFF-Hg can more accurately capture the spatial distribution of Hg pollution near point sources while it reports consistent averaged results with CMAQ-Hg.

*3.2. Source contribution analysis*

*3.2.1. Source contribution analysis of the entire domain*

Fig. 6 shows the seasonal variability of the contributions obtained from the source apportionment modeling of scenarios (BCON, CFPP, MSWI, CEM, NONF, IASP, PM, and OTHER) in the cPRD and the annual contribution distribution maps of different categories to Hg deposition are shown in Fig. S6. The variability of monthly contribution among the evaluated emission sectors is caused by speciation and environmental conditions (e.g. meteorological factors, locations of point sources). Contributions of local sources to deposition in the study domain are larger in the summer months with stronger deposition, whereas the contribution ratio of

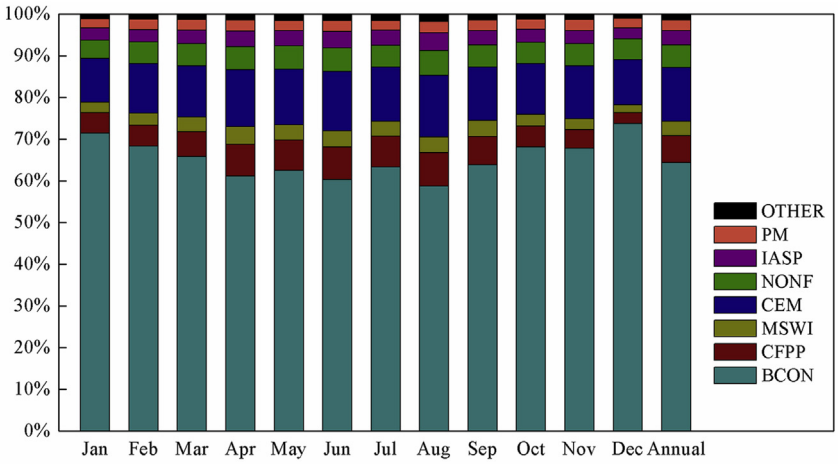


**Fig. 6.** Source contribution of THg deposition to the entire domain by sector categories; BCON: boundary conditions, CFPP: coal-fired power plants, MSWI: municipal solid waste incineration, CEM: cement production, NONF: non-ferrous metal smelting, IASP: iron and steel production, PM: paper-making production, OTHER: other point sources, PS: point source.

BCON is lower with its deposition increased in the wet season. The higher deposition of BCON during the wet season is mainly due to the high oxidation of GEM under increased oxidant concentration and subsequent deposition. However, the greater abundance of the contaminated air mass, which is transported from the northern cities out of the domain, being deposited locally, makes the contribution ratios of BCON relatively higher in winter and early spring. Additionally, the wet depositions of local sources are greatly elevated by precipitation and photochemical activities in the wet season, which is the reason for that the contribution ratios of local sources increased.

From the annual contribution, BCON reaches 64.4%, which indicates the significant contribution of the out-of-domain Hg emissions. As the second most important sector (31.1%) with the highest GOM percentage (35.7%) in the cPRD, CEM correspondingly becomes the highest contributor and constitutes 13.0% of the total deposition. In the remaining sectors, the top three contributors are CFPP (6.5%), NONF (5.4%), and IASP (3.5%). The relative contribution of CFPP and CEM differs from that reported in other literature (Liu et al., 2019; Wang et al., 2014; Zhu et al., 2015); there are primarily three reasons: (1) the Hg speciation is dissimilar for CEM; (2) this paper is based on a smaller study domain and CFPP emission could be transported remotely; (3) some Hg control measures have been applied for CFPP in the cPRD by the end of 2014. Furthermore, it is noteworthy that MSWI contributes 3.4% to Hg deposition, although there are only eight municipal solid waste incinerators. The higher percentage derives from the higher average Hg emission and the higher GOM fraction (12%), which significantly contributes to both dry and wet deposition. Of all uncertainty cases (U1-U12), the results of most cases (U3-U12) have no significant impact on the contribution ratios of categories to the domain's deposition except CFPP. The contribution ratios of U2 show that CFPP (17%) is the largest contributor, followed by CEM (12%). In the U1 case, CEM becomes the most important contributor and the contribution ratio of CFPP reduces to 2%. However, according to the combination of APCDs in CFPP in Guangdong, Hg emission is dominated by GEM, about 70%~80% (Liu et al., 2018). In conclusion, the uncertainties of Hg speciation have little influence on the contribution of sectors to Hg deposition of the domain.

Moreover, the total emission and deposition contributions of all 72 point sources (PS1-PS72, shown in **Fig. 2**) based on the alone deposition results of single point sources are shown in Fig. S7, while the detailed emission and deposition were provided in the Table S8–S13. The THg emission of the 72 large point sources is 7174 kg year$^{-1}$, only about 20% of them deposited in the domain, but accounting for more than 30% of the total deposition caused by all sources in the entire domain. Among the emissions of different species, 3885 kg of GEM emission contribute only 8.1% of the deposition which is caused by 72 point sources due to its long-range transport and few wet depositions. The emission of PBM is not high, but because of its higher wet deposition velocity, the contribution ratio (4.1%) is relatively significant compared with its emission ratio (2.1%). GOM, whose emission accounts for 43.8% of THg emission of 72 point sources, is the dominated contributor to the total deposition. The emission categories with high GOM content, such as MSWI, IASP, and CEM plants (79%, 65%, and 50%, respectively), contribute to substantially greater local deposition. The high GOM ratio corresponds to the deposition contribution ratios of each listed plant of MSWI, IASP, and CEM as being 1.37–1.65, 1.18–1.77, and 1.05–2.08 times of emission contribution ratios, except for a few plants (PS16, PS34, PS37 and PS68) which were located near the border and deposited out of domain. The emission from the 72 point sources of three categories, 44.9% of total emission, was responsible for 56.3% of the deposition. While CFPP has a higher ratio of GEM in Hg emission, it is more likely to be transported farther. Based on the model results (Table S8), only about 1.9% of the GEM discharged from the 21 coal-fired power plants (of 72 point sources) deposited in the domain. It implies that MSWI, IASP, and CEM should be taken as a priority for near-field Hg deposition pollution control because of their deposition quantity, while CFPP with the largest emission should be controlled under the condition of long-range transport and global/intercontinental deposition reduction.

### *3.2.2. Source contribution analysis at high deposition sites*

While quantifying the contribution of the important sectors to regional Hg deposition is necessary for a better understanding of the benefits of emission reduction efforts in a macroscopic perspective, it is of equal significance to identify the contributions of individual sources to high deposition sites for more effective microscopic management. At the 6 investigated receptors, the depositions are more than 3 times of the average deposition of the entire domain; and they are also the top deposition receptors of the several polluted areas (the northern and center of FS, western and northeastern of GZ, etc.). Table S14 shows the contributions to the depositions of 6 selected receptors (RP1-RP6, displayed in Fig. 2)

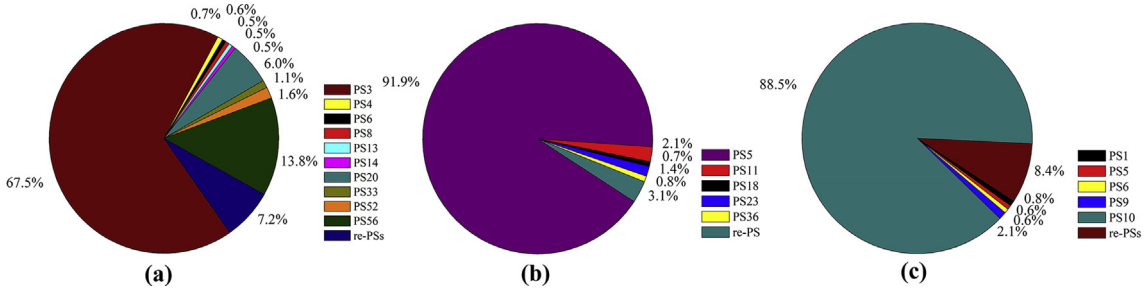


**Fig. 7.** The individual point source's contribution to the three typical receptors: (a) RP3, near the coal-fired power plant (PS3); (b) RP5, near the cement plant (PS5); (c) RP6, near the municipal solid waste incinerator (PS10). PS: point source.

from all 2221 point sources. The contribution ratios of these point sources which have the most important influence on the receptors are 67%–94%. Furthermore, RP3, RP5, and RP6 are further picked as the three most typical receptors of the 6 receptors, due to the fact that they are separately sited around the coal-fired power plant (PS3), the cement plant (PS5) and the municipal solid waste incinerator (PS10) which is the first or second THg emitter in their categories, respectively. These three point sources represent the most important categories to Hg deposition in China and the cPRD region according to the reported literature (Chen et al., 2013a; Liu et al., 2019; Wang et al., 2014; Ying et al., 2017; Zhang et al., 2015) and the associated model results, and they will still be the most influential sectors for Hg deposition in the foreseeable future. The source contribution proportions of the three receptors are shown in Fig. 7. At RP3, several point sources have a relatively significant influence on its Hg deposition due to the location. At RP5 and RP6, there are only five PSs contributing above 0.5%, while the contribution ratios of PS5 to RP5 and PS10 to RP6 were 91.9% and 88.5%, respectively. As can be clearly seen in Table S14 and Fig. 7, the higher depositions occurred mainly depend on the locations that meet the following characteristics: (1) it is near a single maximal point source (e.g., RP1); (2) it is located where there are surrounding large point sources which would have an additive impact (e.g., RP5). The major contributors to depositions of the receptors are the point sources located nearest with highest Hg emission. Overall, the large point sources with large Hg emission, like thermal power generation, municipal solid waste incineration, cement production, and metal smelting, which are, for the most part, intensive energy consumers, have great influence on their nearby areas, accordingly should be the prioritized for application of emission control measures.

## 4. Conclusions

In this study, the CALPUFF was improved to a Hg compatible version CALPUFF-Hg to conduct a simulation of Hg concentration and deposition in a typical industrial zone in cPRD with a grid resolution of 1 km × 1 km, and the contributions of industrial sectors and individual point sources to Hg deposition were evaluated. The model results were verified by comparing available observation, literature data, and CMAQ-Hg results, it predicts that the Hg concentration and deposition are higher near large point sources than CMAQ-Hg results and meet reasonable well with observed data.

The source contribution results obtained from CALPUFF-Hg showed that CEM (13.0%) is the largest contributor to the Hg deposition within the model domain, followed by CFPP (6.5%), NONF (5.4%), IASP (3.5%), and MSWI (3.4%). In addition, the point sources of CEM, IASP, and MSWI are more likely to have an obvious impact on their near-field deposition, due to the relatively higher ratio of GOM in the plume. With respect to higher deposition receptors, the most important contributor is the nearest point source with large Hg emission from them. The CFPP, NONF, and IASP, as the important air pollutant emission sources, have been well controlled by the implementation of "Ultra-Low Emission and Energy Saving of Coal-fired Power Plant Plan" (MEE, 2015b), "Emission Standards of Iron and Steel Industrial Pollutants" (MEE, 2012a, 2012b; 2012c, 2012d) and "Emission Standards of Non-ferrous Metal Smelting Industrial Pollutants" (MEE, 2010, 2014a; 2015a), respectively, in Guangdong. However, CEM and MSWI were rarely highlighted because the previous emission reduction mainly focused on coal combustions. Only in the revised "Emission Standard of Air Pollutants for Cement Industry" (MEE, 2013) in 2013, were Hg and its compounds mentioned as a limit of 0.05 mg $m^{-3}$ during cement manufacturing (while the limit is 0.015 mg $m^{-3}$ in the non-ferrous metal smelting industries). The concentrations of Hg and its compounds were limited to 0.2 mg $m^{-3}$ in the first-ever released emission standard (MEE, 2001) on MSWI and the limitation becomes stringent to 0.05 mg $m^{-3}$ (MEE, 2014b) in the revised and latest version in 2014, but it is still a relatively loose limit in comparison to the sharply increasing amount of incinerated waste in recent years and expected in the near future. Therefore, the reduction of Hg emission in the cPRD region should be a priority for CEM and its emission management should be reinforced. Moreover, the emission reduction of MSWI should be prioritized as well because of its association with economic development and a waste output growth rate of 10% in PRD (Chen et al., 2013a).

Although CALPUFF-Hg has been shown to be capable of simulating the impact of individual PS in a fine resolution, the improvement is still a preliminary effort as only basic chemical reactions are included. While complex transformation may occur because there are relatively higher temperature and high concentrations of pollutants like $NO_x$, HCl, $PM_{2.5}$ in flue gas in and near the discharging port. So these process should be further incorporated into the model and extensive sensitivity analysis should be conducted to evaluate their influences on Hg mass balance near large point sources and also in a regional and global scale.

## Acknowledgements

This work was supported by the Natural Science and Technology Foundation of Guangdong Province, China (2016A020221001), National research program for key issues in air pollution control (No.DQGG0301), The National Key Research and Development Program of China (No.2016YFC0207606), the Fundamental Research Funds for the Central Universities (No.D2160320, D6180330, and D2170150), and Natural Science Foundation of Guangdong Province, China (Nos. 2017A030310279).

## Appendix A. Supplementary data

Supplementary data to this article can be found online at

https://doi.org/10.1016/j.envpol.2019.04.008.

## References


Ariya, P.A., Amyot, M., Dastoor, A., Deeds, D., Feinberg, A., Kos, G., et al., 2015. Mercury physicochemical and biogeochemical transformation in the atmosphere and at atmospheric interfaces: a review and future directions. Chem. Rev. 115 (10), 3760–3802. https://doi.org/10.1021/cr500667e.

Bieser, J., Slemr, F., Ambrose, J., Brenninkmeijer, C., Brooks, S., Dastoor, A., et al., 2017. Multi-model study of mercury dispersion in the atmosphere: vertical and interhemispheric distribution of mercury species. Atmos. Chem. Phys. 17 (11), 6925–6955. https://doi.org/10.5194/acp-17-6925-2017.

Bullock, O.R., Brehme, K.A., 2002. Atmospheric mercury simulation using the CMAQ model: formulation description and analysis of wet deposition results. Atmos. Environ. 36 (13), 2135–2146. https://doi.org/10.1016/s1352-2310(02)00220-0.

Carravieri, A., Fort, J., Tarroux, A., Cherel, Y., Love, O.P., Prieur, S., et al., 2018. Mercury exposure and short-term consequences on physiology and reproduction in Antarctic petrels. Environ. Pollut. 237, 824–831. https://doi.org/10.1016/j.envpol.2017.11.004.

Chen, L., Wang, H.H., Liu, J.F., Tong, Y.D., Ou, L.B., Zhang, W., et al., 2014. Intercontinental transport and deposition patterns of atmospheric mercury from anthropogenic emissions. Atmos. Chem. Phys. 14 (18), 10163–10176. https://doi.org/10.5194/acp-14-10163-2014.

Chen, L., Zhang, W., Zhang, Y.X., Tong, Y.D., Liu, M.D., Wang, H.H., et al., 2018. Historical and future trends in global source-receptor relationships of mercury. Sci. Total Environ. 610, 24–31. https://doi.org/10.1016/j.scitotenv.2017.07.182.

Chen, L.G., Liu, M., Fan, R.F., Ma, S.X., Xu, Z.C., Ren, M.Z., et al., 2013a. Mercury speciation and emission from municipal solid waste incinerators in the Pearl River Delta, South China. Sci. Total Environ. 447, 396–402. https://doi.org/10.1016/j.scitotenv.2013.01.018.

Chen, L.G., Liu, M., Xu, Z.C., Fan, R.F., Tao, J., Chen, D.H., et al., 2013b. Variation trends and influencing factors of total gaseous mercury in the Pearl River Delta-A highly industrialised region in South China influenced by seasonal monsoons. Atmos. Environ. 77, 757–766. https://doi.org/10.1016/j.atmosenv.2013.05.053.

Cheng, I., Xu, X., Zhang, L., 2015. Overview of receptor-based source apportionment studies for speciated atmospheric mercury. Atmos. Chem. Phys. 15 (14), 7877–7895. https://doi.org/10.5194/acp-15-7877-2015.

Cui, H.Y., Chen, W.H., Dai, W., Liu, H., Wang, X.M., He, K.B., 2015. Source apportionment of $PM_{2.5}$ in Guangzhou combining observation data analysis and chemical transport model simulation. Atmos. Environ. 116, 262–271. https://doi.org/10.1016/j.atmosenv.2015.06.054.

De Simone, F., Cinnirella, S., Gencarelli, C.N., Yang, X., Hedgecock, I.M., Pirrone, N., 2015. Model study of global mercury deposition from biomass burning. Environ. Sci. Technol. 49 (11), 6712–6721. https://doi.org/10.1021/acs.est.5b00969.

De Simone, F., Hedgecock, I.M., Carbone, F., Cinnirella, S., Sprovieri, F., Pirrone, N., 2017. Estimating uncertainty in global mercury emission source and deposition receptor relationships. Atmosphere 8 (12), 13. https://doi.org/10.3390/atmos8120236.

Driscoll, C.T., Mason, R.P., Chan, H.M., Jacob, D.J., Pirrone, N., 2013. Mercury as a global pollutant: sources, pathways, and effects. Environ. Sci. Technol. 47 (10), 4967–4983. https://doi.org/10.1021/es305071v.

Fang, F.M., Wang, Q.C., Li, J.F., 2001. Atmospheric particulate mercury concentration and its dry deposition flux in Changchun City, China. Sci. Total Environ. 281 (1–3), 229–236. https://doi.org/10.1016/s0048-9697(01)00849-x.

Feng, X.B., Sommar, J., Lindqvist, O., Hong, Y.T., 2002. Occurrence, emissions and deposition of mercury during coal combustion in the Province Guizhou, China. Water Air Soil Pollut. 139 (1–4), 311–324. https://doi.org/10.1023/a:1015846605651.

Garcia, G.F., Alvarez, H.B., Echeverria, R.S., de Alba, S.R., Rueda, V.M., Dosantos, E.C., et al., 2017. Spatial and temporal variability of atmospheric mercury concentrations emitted from a coal-fired power plant in Mexico. J. Air Waste Manag. Assoc. 67 (9), 973–985. https://doi.org/10.1080/10962247.2017.1314871.

Gbor, P.K., Wen, D.Y., Meng, F., Yang, F.Q., Zhang, B.N., Sloan, J.J., 2006. Improved model for mercury emission, transport and deposition. Atmos. Environ. 40 (5), 973–983. https://doi.org/10.1016/j.atmosenv.2005.10.040.

Gencarelli, C.N., Bieser, J., Carbone, F., De Simone, F., Hedgecock, I.M., Matthias, V., et al., 2017. Sensitivity model study of regional mercury dispersion in the atmosphere. Atmos. Chem. Phys. 17 (1), 627–643. https://doi.org/10.5194/acp-17-627-2017.

Ghannam, K., El-Fadel, M., 2013. A framework for emissions source apportionment in industrial areas: MM5/CALPUFF in a near-field application. J. Air Waste Manag. Assoc. 63 (2), 190–204. https://doi.org/10.1080/10962247.2012.739982.

Guo, Y.N., Feng, X.B., Li, Z.G., He, T.R., Yan, H.Y., Meng, B., et al., 2008. Distribution and wet deposition fluxes of total and methyl mercury in Wujiang River Basin, Guizhou, China. Atmos. Environ. 42 (30), 7096–7103. https://doi.org/10.1016/j.atmosenv.2008.06.006.

Guangzhou Environmental Protection (GZEP), 2013. Guangzhou Environment Bulletin of 2012. GZEP, Guangzhou, China [In Chinese]. Retrieved from. http://www.gzepb.gov.cn/zwgk/hjgb/201306/t20130621_53601.htm.

Heckel, P.F., LeMasters, G.K., 2011. The use of AERMOD air pollution dispersion models to estimate residential ambient concentrations of elemental mercury. Water Air Soil Pollut. 219 (1–4), 377–388. https://doi.org/10.1007/s11270-010-0714-4.

Holmes, C.D., Jacob, D.J., Corbitt, E.S., Mao, J., Yang, X., Talbot, R., et al., 2010. Global atmospheric model for mercury including oxidation by bromine atoms. Atmos. Chem. Phys. 10 (24), 12037–12057. https://doi.org/10.5194/acp-10-12037-2010.

Hong, Q.Q., Xie, Z.Q., Liu, C., Wang, F.Y., Xie, P.H., Kang, H., et al., 2016. Speciated atmospheric mercury on haze and non-haze days in an inland city in China. Atmos. Chem. Phys. 16 (21), 13807–13821. https://doi.org/10.5194/acp-16-13807-2016.

Horowitz, H.M., Jacob, D.J., Zhang, Y.X., Dibble, T.S., Slemr, F., Amos, H.M., et al., 2017. A new mechanism for atmospheric mercury redox chemistry: implications for the global mercury budget. Atmos. Chem. Phys. 17 (10), 6353–6371. https://doi.org/10.5194/acp-17-6353-2017.

Huang, M.J., Deng, S.X., Dong, H.Y., Dai, W., Pang, J.M., Wang, X.M., 2016. Impacts of atmospheric mercury deposition on human multimedia exposure: projection from observations in the Pearl River Delta region, South China. Environ. Sci. Technol. 50 (19), 10625–10634. https://doi.org/10.1021/acs.est.6b00514.

Kos, G., Ryzhkov, A., Dastoor, A., Narayan, J., Steffen, A., Ariya, P.A., et al., 2013. Evaluation of discrepancy between measured and modelled oxidized mercury species. Atmos. Chem. Phys. 13 (9), 4839–4863. https://doi.org/10.5194/acp-13-4839-2013.

Kwok, R.H.F., Baker, K.R., Napelenok, S.L., Tonnesen, G.S., 2015. Photochemical grid model implementation and application of VOC, $NO_x$, and $O_3$ source apportionment. Geosci. Model Dev. (GMD) 8 (1), 99–114. https://doi.org/10.5194/gmd-8-99-2015.

Landis, M.S., Keeler, G.J., Al-Wali, K.I., Stevens, R.K., 2004. Divalent inorganic reactive gaseous mercury emissions from a mercury cell chlor-alkali plant and its impact on near-field atmospheric dry deposition. Atmos. Environ. 38 (4), 613–622. https://doi.org/10.1016/j.atmosenv.2003.09.075.

Li, Z., Xia, C.H., Wang, X.M., Xiang, Y.R., Xie, Z.Q., 2011. Total gaseous mercury in Pearl River Delta region, China during 2008 winter period. Atmos. Environ. 45 (4), 834–838. https://doi.org/10.1016/j.atmosenv.2010.11.032.

Lin, C.J., Pan, L., Streets, D.G., Shetty, S.K., Jang, C., Feng, X., et al., 2010. Estimating mercury emission outflow from East Asia using CMAQ-Hg. Atmos. Chem. Phys. 10 (4), 1853–1864. https://doi.org/10.5194/acp-10-1853-2010.

Lin, C.J., Pehkonen, S.O., 1999. The chemistry of atmospheric mercury: a review. Atmos. Environ. 33 (13), 2067–2079. https://doi.org/10.1016/s1352-2310(98)00387-2.

Lin, C.J., Pongprueks, P., Rusell Bulock, O., Lindberg, S.E., Pehkonen, S.O., Jang, C., et al., 2007. Scientific uncertainties in atmospheric mercury models II: sensitivity analysis in the CONUS domain. Atmos. Environ. 41 (31), 6544–6560. https://doi.org/10.1016/j.atmosenv.2007.04.030.

Lin, C.J., Pongprueksa, P., Lindberg, S.E., Pehkonen, S.O., Byun, D., Jang, C., 2006. Scientific uncertainties in atmospheric mercury models I: model science evaluation. Atmos. Environ. 40 (16), 2911–2928. https://doi.org/10.1016/j.atmosenv.2006.01.009.

Lin, C.J., Shetty, S.K., Pan, L., Pongprueksa, P., Jang, C., Chu, H.W., 2012. Source attribution for mercury deposition in the contiguous United States: regional difference and seasonal variation. J. Air Waste Manag. Assoc. 62 (1), 52–63. https://doi.org/10.1080/10473289.2011.622066.

Liu, J.J., Wang, L., Zhu, Y., Lin, C.J., Jang, C., Wang, S.X., et al., 2019. Source attribution for mercury deposition with an updated atmospheric mercury emission inventory in the Pearl River Delta Region, China. Front. Environ. Sci. Eng. 13 (1), 14. https://doi.org/10.1007/s11783-019-1087-6.

Ma, Y.F., Lu, K.D., Chou, C.C.K., Li, X.Q., Zhang, Y.H., 2017. Strong deviations from the NO-NO2-O-3 photostationary state in the Pearl River Delta: Indications of active peroxy radical and chlorine radical chemistry. Atmos. Environ. 163, 22–34. https://doi.org/10.1016/j.atmosenv.2017.05.012.

Massman, W.J., 1999. Molecular diffusivities of Hg vapor in air, $O_2$ and $N_2$ near STP and the kinematic viscosity and thermal diffusivity of air near STP. Atmos. Environ. 33 (3), 453–457. https://doi.org/10.1016/s1352-2310(98)00204-0.

Ministry of Ecology and Environment of the People's Republic of China (MEE), 2001. Standard for Pollution Control on the Municipal Solid Waste Incineration. MEE, Beijing, China [In Chinese]. Retrieved from http://www.mee.gov.cn/home/ztbd/rdzl/yjcz/bzgf/201106/t20110601_211493.shtml.

Ministry of Ecology and Environment of the People's Republic of China (MEE), 2009. Notice on Carrying Out the Investigation of the Dynamic Update of Pollution Source Census. MEE, Beijing, China [In Chinese]. Retrieved from http://www.mee.gov.cn/gkml/hbb/bwj/201001/t20100111_184084.htm.

Ministry of Ecology and Environment of the People's Republic of China (MEE), 2010. Emission Standard of Pollutants for Lead Anf Zinc Industry. MEE, Beijing, China [In Chinese]. Retrieved from http://kjs.mee.gov.cn/hjbhbz/bzwb/shjbh/swrwpfbz/201010/t20101009_195340.shtml.

Ministry of Ecology and Environment of the People's Republic of China (MEE), 2012a. Emission Standard of Air Pollutants for Iron Smelt Industry. MEE, Beijing, China [In Chinese]. Retrieved from http://kjs.mee.gov.cn/hjbhbz/bzwb/dqhjbh/dqgdwrywrwpfbz/201207/t20120731_234141.shtml.

Ministry of Ecology and Environment of the People's Republic of China (MEE), 2012b. Emission Standard of Air Pollutants for Steel Rolling Industry. MEE, Beijing, China [In Chinese]. Retrieved from http://kjs.mee.gov.cn/hjbhbz/bzwb/dqhjbh/dqgdwrywrwpfbz/201207/t20120731_234143.shtml.

Ministry of Ecology and Environment of the People's Republic of China (MEE), 2012c. Emission Standard of Air Pollutants for Steel Smelt Industry. MEE, Beijing, China [In Chinese]. Retrieved from http://kjs.mee.gov.cn/hjbhbz/bzwb/dqhjbh/dqgdwrywrwpfbz/201207/t20120731_234142.shtml.

Ministry of Ecology and Environment of the People's Republic of China (MEE), 2012d. Emission Standard of Pollutants for Ferrolloy Smelt Industry. MEE, Beijing, China [In Chinese]. Retrieved from http://kjs.mee.gov.cn/hjbhbz/bzwb/

shjbh/swrwpfbz/201207/t20120731_234145.shtml.
Ministry of Ecology and Environment of the People's Republic of China (MEE), 2013. Emission Standard of Air Pollutants for Cement Industry. MEE, Beijing, China [In Chinese]. Retrieved from http://kjs.mee.gov.cn/hjbhbz/bzwb/dqhjbh/dqgdwrywrwpfbz/201312/t20131227_265765.shtml.
Ministry of Ecology and Environment of the People's Republic of China (MEE), 2014a. Emission Standards of Pollutants for Stannum, Antimony and Mercury Industry. MEE, Beijing, China [In Chinese]. Retrieved from http://kjs.mee.gov.cn/hjbhbz/bzwb/dqhjbh/dqgdwrywrwpfbz/201405/t20140530_276308.shtml.
Ministry of Ecology and Environment of the People's Republic of China (MEE), 2014b. Standard for Pollution Control on the Municipal Solid Waste Incineration. MEE, Beijing, China [In Chinese]. Retrieved from http://kjs.mee.gov.cn/hjbhbz/bzwb/gthw/gtfwwrkzbz/201405/t20140530_276307.shtml.
Ministry of Ecology and Environment of the People's Republic of China (MEE), 2015a. Emission Standards of Pollutants for Secondary Copper, Aluminum, Lead and Zink Industry. MEE, Beijing, China [In Chinese]. Retrieved from http://kjs.mee.gov.cn/hjbhbz/bzwb/dqhjbh/dqgdwrywrwpfbz/201505/t20150505_300588.shtml.
Ministry of Ecology and Environment of the People's Republic of China (MEE), 2015b. Implementation Plan of Ultra-low Emission and Energy Saving of Coal-Fired Power Plant ([In Chinese]).
Michael, R., Stuart, A.L., Trotz, M.A., Akiwumi, F., 2016. Source apportionment of wet-deposited atmospheric mercury in Tampa, Florida. Atmos. Res. 170, 168–175. https://doi.org/10.1016/j.atmosres.2015.11.017.
Pacyna, J.M., Travnikov, O., De Simone, F., Hedgecock, I.M., Sundseth, K., Pacyna, E.G., et al., 2016. Current and future levels of mercury atmospheric pollution on a global scale. Atmos. Chem. Phys. 16 (19), 12495–12511. https://doi.org/10.5194/acp-16-12495-2016.
Pai, P., Karamchandani, P., Seigneur, C., 2000. On artificial dilution of point source mercury emissions in a regional atmospheric model. Sci. Total Environ. 259 (1–3), 159–168. https://doi.org/10.1016/s0048-9697(00)00579-9.
Pongprueksa, P., Lin, C.J., Lindberg, S.E., Jang, C., Braverman, T., Bullock, O.R., et al., 2008. Scientific uncertainties in atmospheric mercury models III: boundary and initial conditions, model grid resolution, and Hg(II) reduction mechanism. Atmos. Environ. 42 (8), 1828–1845. https://doi.org/10.1016/j.atmosenv.2007.11.020.
Risch, M.R., DeWild, J.F., Gay, D.A., Zhang, L.M., Boyer, E.W., Krabbenhoft, D.P., 2017. Atmospheric mercury deposition to forests in the eastern USA. Environ. Pollut. 228, 8–18. https://doi.org/10.1016/j.envpol.2017.05.004.
Rolfhus, K.R., Sakamoto, H.E., Cleckner, L.B., Stoor, R.W., Babiarz, C.L., Back, R.C., et al., 2003. Distribution and fluxes of total and methylmercury in Lake Superior. Environ. Sci. Technol. 37 (5), 865–872. https://doi.org/10.1021/es026065e.
Ryaboshapko, A., Bullock, R., Ebinghaus, R., Ilyin, I., Lohman, K., Munthe, J., et al., 2002. Comparison of mercury chemistry models. Atmos. Environ. 36 (24), 3881–3898. https://doi.org/10.1016/s1352-2310(02)00351-5.
Shetty, S.K., Lin, C.J., Streets, D.G., Jang, C., 2008. Model estimate of mercury emission from natural sources in East Asia. Atmos. Environ. 42 (37), 8674–8685. https://doi.org/10.1016/j.atmosenv.2008.08.026.
Sigler, J.M., Mao, H., Talbot, R., 2009. Gaseous elemental and reactive mercury in Southern New Hampshire. Atmos. Chem. Phys. 9 (6), 1929–1942. https://doi.org/10.5194/acp-9-1929-2009.
Sung, J.H., Roy, D., Oh, J.S., Back, S.K., Jang, H.N., Kim, S.H., et al., 2018. Transboundary movement of mercury in the Northeast Asian region predicted by CAMQ-Hg from anthropogenic emissions distribution. Atmos. Res. 203, 197–206. https://doi.org/10.1016/j.atmosres.2017.12.015.
Travnikov, O., Angot, H., Artaxo, P., Bencardino, M., Bieser, J., D'Amore, F., et al., 2017. Multi-model study of mercury dispersion in the atmosphere: atmospheric processes and model evaluation. Atmos. Chem. Phys. 17 (8), 5271–5295. https://doi.org/10.5194/acp-17-5271-2017.
Voudouri, A., Kallos, G., 2007. Validation of the integrated RAMS-Hg modelling system using wet deposition observations for eastern North America. Atmos. Environ. 41 (27), 5732–5745. https://doi.org/10.1016/j.atmosenv.2007.02.045.
Wang, L., Wang, S.X., Zhang, L., Wang, Y.X., Zhang, Y.X., Nielsen, C., et al., 2014. Source apportionment of atmospheric mercury pollution in China using the GEOS-Chem model. Environ. Pollut. 190, 166–175. https://doi.org/10.1016/j.envpol.2014.03.011.
Wang, X., Bao, Z.D., Lin, C.J., Yuan, W., Feng, X.B., 2016a. Assessment of global mercury deposition through litterfall. Environ. Sci. Technol. 50 (16), 8548–8557. https://doi.org/10.1021/acs.est.5b06351.
Wang, X., Lin, C.J., Feng, X.B., Yuan, W., Fu, X.W., Zhang, H., et al., 2018. Assessment of regional mercury deposition and emission outflow in mainland China. J. Geophys. Res. Atmos. 123 (17), 9868–9890. https://doi.org/10.1029/2018jd028350.
Wang, X., Lin, C.J., Yuan, W., Sommar, J., Zhu, W., Feng, X.B., 2016b. Emission-dominated gas exchange of elemental mercury vapor over natural surfaces in China. Atmos. Chem. Phys. 16 (17), 11125–11143. https://doi.org/10.5194/acp-16-11125-2016.
Wu, H., Zhang, Y., Yu, Q., Ma, W.C., 2018. Application of an integrated Weather Research and Forecasting (WRF)/CALPUFF modeling tool for source apportionment of atmospheric pollutants for air quality management: a case study in the urban area of Benxi, China. J. Air Waste Manag. Assoc. 68 (4), 347–368. https://doi.org/10.1080/10962247.2017.1391009.
Wu, Q.R., Wang, S.X., Li, G.L., Liang, S., Lin, C.J., Wang, Y.F., et al., 2016. Temporal trend and spatial distribution of speciated atmospheric mercury emissions in China during 1978-2014. Environ. Sci. Technol. 50 (24), 13428–13435. https://doi.org/10.1021/acs.est.6b04308.
Xu, L.L., Chen, J.S., Yang, L.M., Yin, L.Q., Yu, J.S., Qiu, T.X., et al., 2014. Characteristics of total and methyl mercury in wet deposition in a coastal city, Xiamen, China: concentrations, fluxes and influencing factors on Hg distribution in precipitation. Atmos. Environ. 99, 10–16. https://doi.org/10.1016/j.atmosenv.2014.09.054.
Xu, X.H., Yang, X.S., Miller, D.R., Helble, J.J., Carley, R.J., 2000. A regional scale modeling study of atmospheric transport and transformation of mercury. I. Model development and evaluation. Atmos. Environ. 34 (28), 4933–4944. https://doi.org/10.1016/s1352-2310(00)00228-4.
Yang, W., Zhu, Y., Jang, C., Long, S., Lin, C.-J., Yu, B., et al., 2018a. Development and case study of a new-generation model-VAT for analyzing the boundary conditions influence on atmospheric mercury simulation. Front. Environ. Sci. Eng. 12 (1) https://doi.org/10.1007/s11783-018-1010-6, 13 (10 pp.)-13 (10 pp.).
Yang, W., Zhu, Y., Jang, C., Shicheng, L., Che-Jen, L., Bin, Y., et al., 2018b. Development and case study of a new-generation model-VAT for analyzing the boundary conditions influence on atmospheric mercury simulation. Front. Environ. Sci. Eng. 12 (1) https://doi.org/10.1007/s11783-018-1010-6, 13 (10 pp.)-13 (10 pp.).
Ye, Z.Y., Mao, H.T., Driscoll, C.T., Wang, Y., Zhang, Y.X., Jaegle, L., 2018. Evaluation of CMAQ coupled with a state-of-the-art mercury chemical mechanism (CMAQ-newHg-Br). J. Adv. Model. Earth Syst. 10 (3), 668–690. https://doi.org/10.1002/2017ms001161.
Ying, H., Deng, M.H., Li, T.Q., Jan, J.P.G., Chen, Q.Q., Yang, X.E., et al., 2017. Anthropogenic mercury emissions from 1980 to 2012 in China. Environ. Pollut. 226, 230–239. https://doi.org/10.1016/j.envpol.2017.03.059.
Zhang, L., Wang, S.X., Wang, L., Wu, Y., Duan, L., Wu, Q.R., et al., 2015. Updated emission inventories for speciated atmospheric mercury from anthropogenic sources in China. Environ. Sci. Technol. 49 (5), 3185–3194. https://doi.org/10.1021/es504840m.
Zhang, Y., Wang, W., Wu, S.Y., Wang, K., Minoura, H., Wang, Z.F., 2014. Impacts of updated emission inventories on source apportionment of fine particle and ozone over the southeastern US. Atmos. Environ. 88, 133–154. https://doi.org/10.1016/j.atmosenv.2014.01.035.
Zhao, L.S., Xu, L.L., Wu, X., Zhao, G.Q., Jiao, L., Chen, J.S., et al., 2018. Characteristics and sources of mercury in precipitation collected at the urban, suburban and rural sites in a city of Southeast China. Atmos. Res. 211, 21–29. https://doi.org/10.1016/j.atmosres.2018.04.019.
Zhou, H., Hopke, P.K., Zhou, C., Holsen, T.M., 2019. Ambient mercury source identification at a New York State urban site: rochester, NY. Sci. Total Environ. 650 (Pt 1), 1327–1337. https://doi.org/10.1016/j.scitotenv.2018.09.040.
Zhu, J., Wang, T., Bieser, J., Matthias, V., 2015. Source attribution and process analysis for atmospheric mercury in eastern China simulated by CMAQ-Hg. Atmos. Chem. Phys. 15 (15), 8767–8779. https://doi.org/10.5194/acp-15-8767-2015.
Zhu, J., Wang, T., Talbot, R., Mao, H., Yang, X., Fu, C., et al., 2014. Characteristics of atmospheric mercury deposition and size-fractionated particulate mercury in urban Nanjing, China. Atmos. Chem. Phys. 14 (5), 2233–2244. https://doi.org/10.5194/acp-14-2233-2014.